To cite this version :

Gérard VIGNOLES, Olivia COINDREAU, Dominique BERNARD, Azita AHMADI-SENICHAULT - Assessment of geometrical and transport properties of a fibrous C/C composite preform as digitized by X-ray CMT. Part II: heat and gas transport properties - Journal of Materials Research - Vol. 22, n°6, p.1537-1550 - 2007

Assessment of geometrical and transport properties of a fibrous C/C composite preform as digitized by x-ray computerized microtomography: Part II. Heat and gas transport properties

Gerard L. Vignoles[a] and Olivia Coindreau
Université Bordeaux 1, Laboratoire des Composites ThermoStructuraux (LCTS) 3, Allée La Boëtie, F33600 Pessac, France

Azita Ahmadi
Université Bordeaux 1, Transport, Ecoulements Fluides, Energétique (TREFLE), Esplanade des Arts et Métiers, F33405 Talence, France

Dominique Bernard
Centre National de la Recherche Scientifique (CNRS), Institut de Chimie de la Matière Condensée de Bordeaux (ICMCB), 26 Avenue du Dr. Schweitzer, F33608 Pessac Cedex, France

Raw and partially infiltrated carbon–carbon composite preforms have been scanned by high-resolution synchrotron radiation x-ray computerized microtomography. Three-dimensional high-quality images of the pore space have been produced at two distinct resolutions and have been used for the computation of transport properties: heat conductivity, binary gas diffusivities, Knudsen diffusivities, and viscous flow permeabilities. The computation procedures are based on a double change-of-scale strategy suited to the bimodal nature of pore space and on the local determination of transport anisotropy. Good agreement has been found between all calculated quantities and experimental data.

I. INTRODUCTION

Thermostructural composites are characterized by their ability to operate under high mechanical stresses and high temperature (above 1000 °C), such as in spatial propulsion systems or aircraft brake disks. They are made of carbon or ceramic fibers (SiC, Al_2O_3, etc.) linked together by a carbon or ceramic matrix. The association of these two brittle components leads to a material with pseudoplastic mechanical behavior. They are manufactured, among other processes, by chemical vapor infiltration (CVI): a heated fibrous preform is infiltrated by the chemical cracking of a vapor precursor of the matrix material inside its pore space.[1,2] The final quality of materials fabricated by CVI relies on processing conditions (such as vapor precursor concentration, temperature and pressure), as well as on geometrical, gas and heat transport properties of the preform. This rather expensive process has a strong need for model-based optimization, either in isothermal or in thermal-gradient process modifications. Numerous previous works have shown the crucial importance of adequate structural models in the quality of the modeling procedures.[3–9] In addition to these process-related issues, thermal characteristics of these composites are also of great interest: in some cases (braking, re-entry into the atmosphere, etc.) they are as important as their mechanical or chemical properties.

The aim of the present work is to provide for fibrous carbon/carbon (C/C) composites estimates of such properties based on accurate three-dimensional (3D) representations obtained by x-ray computerized microtomography (CMT). In a previous study, it was demonstrated that geometrical properties of the composite preform could be determined from such images.[10] In this companion paper, the same 3D images are used to assess heat and gas transport properties.

Experimental determination of heat[11–13] and gas[14,15] transport properties of thermostructural composites can be performed. However, this characterization has to be undertaken each time a new material is produced. Moreover, measuring the effective diffusivity of porous media is still a challenging task.[15] To complete these approaches, numerous works have been performed to compute thermal conductivity,[16–19] diffusivity,[20–22] and permeability[23–25] of ideal media such as regular or random

arrays of cylinders. However, real composites exhibit a much more complex structure. In this paper, 3D CMT images are directly used to compute the transport properties of a preform at different stages of densification with the aim of performing direct comparisons with either experimental data or known model results.

In high-resolution images, carbon fibers can be seen in detail whereas low-resolution images enable us to view components of the fibrous reinforcement (yarns and needlings). Our computational method, described in the next paragraph, makes use of low-resolution images to compute thermal conductivity, gas diffusivity, and permeability of the material. High-resolution images are also used to determine the local arrangement of fibers inside yarns and to compute diffusivity–porosity relations. Results related to each property are presented and discussed in Sec. III.

II. EXPERIMENTAL

A thorough description of the material studied here can be found in our previous paper.[10] It is a C/C composite, provided by Snecma Propulsion Solide, Le Haillan, France. The preform weave layers are stacked horizontally (x-y plane). Then, harpoon-shaped needles are used to punch these cloth stacks: as a consequence, fibers are broken and partially transferred in the z direction. The stacks are now held together by the transferred fibers. The volume fraction of fibers is about 30%, and 4% lie in z direction. The diameter of carbon fibers is about 8 μm. The yarn, less than 1 mm in diameter, is made up of the gathering of a large number of fibers. In this study, pores inside a yarn will be referred to as micropores while pores between yarns will be called macropores. Thus, there are two scales of heterogeneity to take into account to correctly assess the properties of the preform.

Three samples were extracted from the preform at different stages of densification. The first one, CC0, was taken from the raw preform. Its bulk density, obtained by weighing and measuring the sample, is 470 kg m^{-3}, and the corresponding porosity is 73%. Two other samples were taken after the preform was partially infiltrated. Because of the fabrication process (isothermal isobaric CVI), the core of the preform is more porous than its borders.

The samples, extracted at different depths, have consequently distinct characteristics. CC1 has a bulk density of 770 kg m^{-3} (corresponding to 58% porosity) and CC2 a bulk density of 1520 kg m^{-3} (corresponding to 20% porosity). The samples were embedded in organic resin and manufactured so they could be imaged at two different resolutions (high and low) and the two scales of porosity could be viewed. In addition to these samples, another sample with an infiltration level intermediate between CC1 and CC2 (giving a 35% porosity) was

imaged only at low resolution. It will be referred to as CC1b.

Refer to the preceding paper[10] for a detailed description of the experimental procedure featuring sample preparation and synchrotron x-ray CMT acquisition at the European Synchrotron Radiation Facility (ESRF, Grenoble, France). Images used in this study are high- and low-resolution images (effective voxel size equal respectively to 0.7 and 7.46 μm). Figure 1 is an example of the results obtained for sample CC1.

III. COMPUTATIONAL METHODS, RESULTS, AND DISCUSSION

A. Double change of scale strategy

Due to the fabrication process (gathering of a large number of fibers in yarns and then partial transfer of fibers in z direction), the preform exhibits two scales of heterogeneity. High-resolution images enable us to view small-scale details [at the scale of the yarn, see Fig. 1(b)] whereas large-scale patterns can be fully captured in low-resolution images [see Fig. 1(a)]. Geometrical assessments[10] strongly support such evidence, at least for partially infiltrated samples. Because low-resolution images provide information only on large-scale properties [i.e., at the representative elementary volume (REV) size], small-scale information must be integrated into it. This is
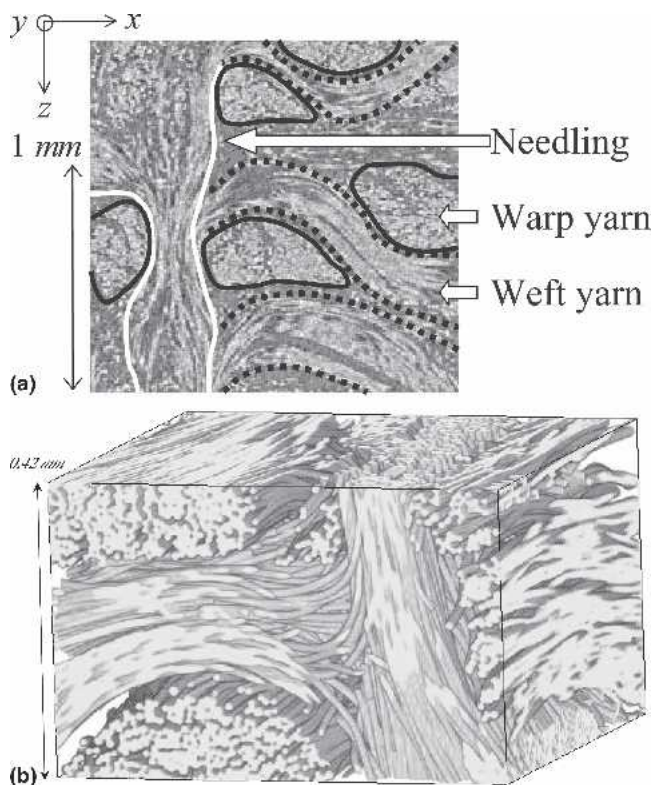

FIG. 1. (a) Rendering of extracts from reconstructed and segmented image CC1. (b) High-resolution 3D volume.

the first change of scale: its procedure, schematized in Fig. 2, consists of determining the local properties of the high-resolution image by dividing it into cubic subsamples of edge length a (variable parameter). Porosity, fiber orientation, and then transport properties inside each subsample are determined. The results are cast into expressions relating the transverse and parallel properties to the local porosity. The second change of scale consists of computing the effective properties (thermal conductivity, gas diffusivity, and permeability) of the low-resolution image from a field of small-scale properties by the method of volume averaging (see Fig. 3). The procedure starts from the subdivision of the low-resolution images into subimages; then, inside every subimage, an evaluation of porosity and local fiber orientation is performed. Then, local property tensors may be affected to every subimage; they may come either from the results of the first change of scale, or from analytical models.

This strategy is suggested by the following argument: in a macroscale image, there exists a distribution of porosity $N(\epsilon)d\epsilon$ that may be assessed by means of image

analysis. If some property Ψ is known to be correlated to porosity by a relation $\Psi = \Psi(\epsilon)$, a porosity-average of the property is given by

$$\langle \psi \rangle^\epsilon = \int_0^1 \psi(\epsilon)N(\epsilon)d\epsilon \quad . \tag{1}$$

Then the proposed procedure is a mere extension of this simple averaging by taking into account the true space distribution of porosity, as sampled at the macroscale. The hypothesis that is taken here is that the porosity–property correlation is correctly sampled at the microscale and directly transposable for macroscale computations.

The double change of scale procedure is suggested for the computation of effective properties of the fibrous preform at the beginning of the densification process (samples CC0 and CC1 with respective porosities 73% and 58%). In the latter stages of densification, a simple change of scale procedure for the computation of gas transport properties is proposed (samples CC1b and CC2
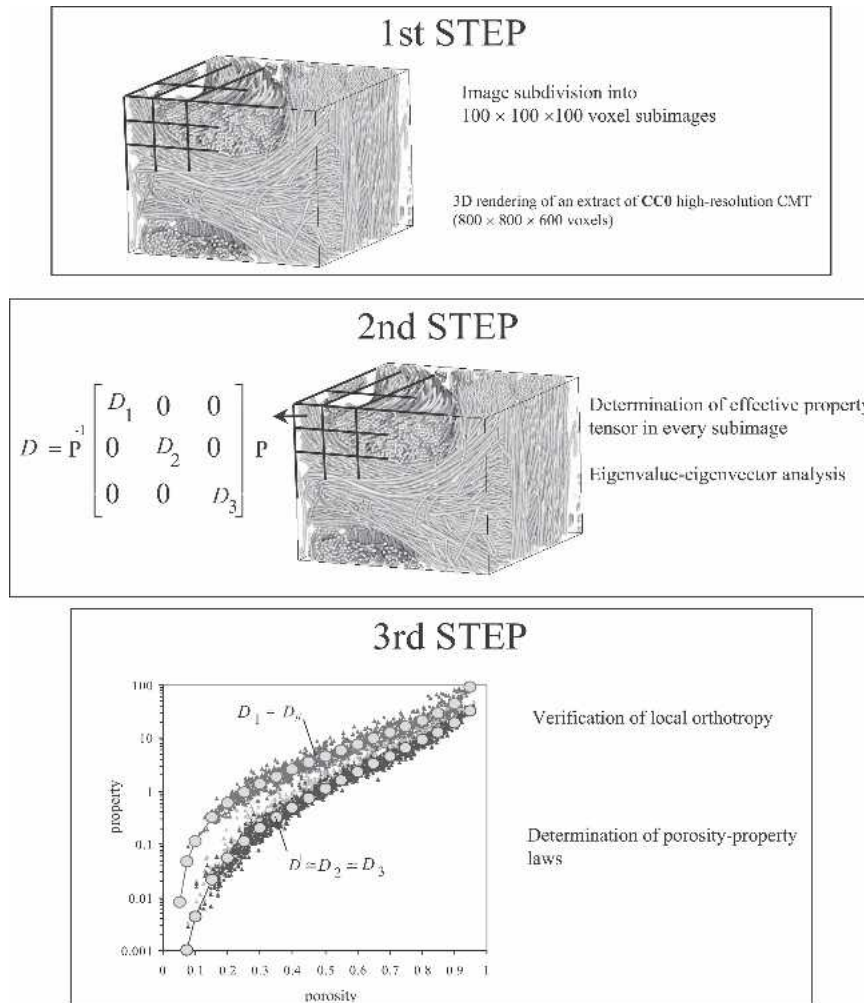

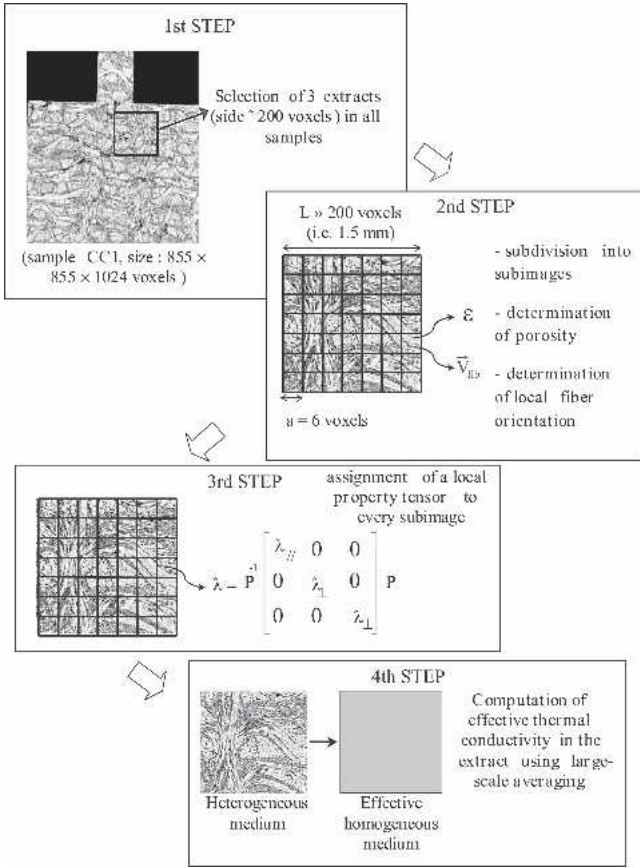FIG. 2. Strategy for a first change of scale.

FIG. 3. Strategy for a second change of scale.

with respective porosities 35% and 20%). Indeed, in such a case, the micropores are quite sealed off by the deposition reaction, so they may be safely disregarded.

B. Determination of local porosity

Six subsamples, 210^3 voxels (i.e., 1.6^3 mm^3) in size, have been selected, three of them in the tomographic low-resolution image of CC0 and the three other ones in the low-resolution image of CC1. Each subsample has been subdivided into cubic sub-subsamples of 6 voxels edge size (i.e., 0.045 mm^3), the porosity of which must be determined. The tomographic image is a 3D reconstruction of the absorption coefficient of the material traversed by the x-ray beam. Therefore, the gray level of each voxel is a linear combination of the average gray level of each individual component of the material. Let G_1 be the gray level associated to void space, and G_2 the gray level of the carbon components (fiber or deposit). Then, the average gray level $\langle G \rangle_i$ of the ith subsample of porosity ϵ_i is

$$\langle G \rangle_i = \epsilon_i\, G_1 + (1 - \epsilon_i)\, G_2 \quad . \tag{2}$$

Finally, a proportionality relationship is given between the average gray level of the sub-subsample and its porosity:

$$\epsilon_i = \frac{1}{G_1 - G_2} \times \langle G \rangle_i - \frac{G_2}{G_1 - G_2} \quad . \tag{3}$$

However, there is a phase contrast phenomenon[26] that makes this law not exactly true. Moreover, we have assumed that the gray level was the same for all carbon-containing components, which is not strictly the case, as their densities are indeed somewhat different.[27] Instead of using Eq. (3), we have determined, in an image of 500 voxels edge length, the threshold grayscale value G_t that leads to a binary image whose porosity matches the experimentally determined value. Then, the porosity ϵ_i of each subimage of 6 voxels edge length has been determined by a thresholding operation at grayscale level G_t. A linear correlation has finally been established between ϵ_i and the average value of the grayscale level $\langle G \rangle_i$ of the subimage.

Using these correlations, the porosity of each sub-sub-sample inside low-resolution images of CC0 and CC1 has been calculated. The mean pore volume fraction of the whole subsamples (210 voxels edge length) are 72.7%, 73.6%, and 73.4% for CC0 and 60.6%, 58.7%, and 55.3% for CC1, in agreement with measurements (73 ± 1.5% for CC0 and 58 ± 2% for CC1). The scatter of pore fraction values indicates that the subsamples are not large enough to be representative, particularly for CC1. Consequently, the effective property of the composite will be assessed by averaging the values determined in the three subsamples.

C. Determination of local fiber orientation

The second geometrical property that is crucial in the computational procedures is the local orientation of the fibers. This issue has been addressed with an original method based on a random-walk algorithm sensitive to the local anisotropy. Details are given in the first part of this article.[10] Each cubic region of 6 voxels edge length was arbitrarily thresholded to 50% pore fraction, and random walkers were allowed to travel in the "fluid" phase until the covariance matrix of the centered displacements, divided by twice the walk time, converged to a pseudodiffusion tensor. The eigenvector associated with the largest eigenvalue indicates the direction of preferred diffusion, which is assimilated to the local fiber orientation. The validity of the method has been checked by quantifying the proportion of fibers lying in the x, y, and z orientations. The proportion detected by our method is in good agreement with values established in other ways.[28]

D. First change of scale by direct computation

Once the porosity and the fiber orientation inside each sub-subsample of 6 voxels edge length were computed, the next step consisted of determining effective transport properties from each subsample by homogenisation.

1. Determination of local gas transport properties

Computations make use of a random-walk algorithm described by Vignoles.[29] It is indeed a homogenization procedure since the effective property is computed over walks, the size of which is much larger than one single image. When a walker crosses an image border, it is reintroduced in the opposite border. Another way to describe the method is to consider that the space is paved by repetition of the elementary image. At $t = 0$, all walkers are placed randomly in the fluid phase of an elementary image located at the space origin: thus the initial average concentration field is (up to some noise due to the finite number of walkers) a hat-function. The random walk provides a numerical Lagrangian solver for the classical unsteady diffusion problem represented by Fick's second law, subject to the above-mentioned initial condition and to boundary conditions of null concentration at infinite distances. The diffusion coefficient that arises from the convergence of the covariance matrix is also an inverse identification of the analytical Gaussian solution in the limit of large spreading (i.e., such that the initial hat-function is considered as a Dirac impulse distribution).

There are three diffusion regimes depending on the Knudsen number Kn, which is the ratio between the mean free path of the molecules and the pore diameter: the ordinary (continuum) regime ($Kn \ll 1$), the transition regime ($Kn \sim 1$) and the Knudsen regime ($Kn \gg 1$). The random walk performed by the molecules introduced in the void space of the porous medium is directly linked to the Knudsen number and allows the effective diffusivity tensor $\underline{D}$ to be determined at any value of Kn.

The numerical procedure, applied with 10,000 walkers over 20,000 voxel-long walks (the image edge size was 141 voxels) has been validated in comparison with analytical results[16] in the bulk diffusion regime for square and hexagonal regular arrays of parallel cylinders and by comparing with numerical results in Knudsen regime for a square array of parallel cylinders[22] with differences inferior to 5% in all cases, the worst ones lying close to the percolation threshold.

Results are shown in Figs. 4 and 5 in terms of tortuosities for Knudsen and ordinary transport in transverse direction. Tortuosity $\underline{\eta}$ is defined by

$$\underline{\eta} = \epsilon D^{\mathrm{ref}} \, \underline{\underline{D}}^{-1} \quad , \tag{4}$$

where D^{ref} is a reference diffusivity, corresponding to the longitudinal diffusivity in a capillary, the diameter of which is equal to the mean pore diameter. This reference value is computed using the Bosanquet formula.[30] When Kn has appreciable values, D^{ref} depends on an assessment of the pore diameter, which is available in the images shown previously.[10]

The results are then collected together in a porosity-transport property correlation.[31] To do so, gas diffusivity
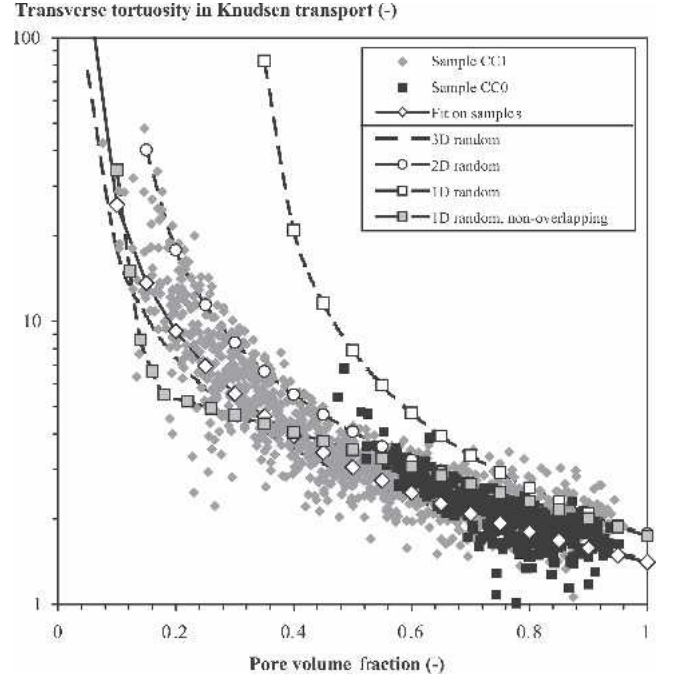

FIG. 4. Tortuosity–porosity correlation plots for Knudsen transport in transverse direction. Comparison of CMT data with established laws.
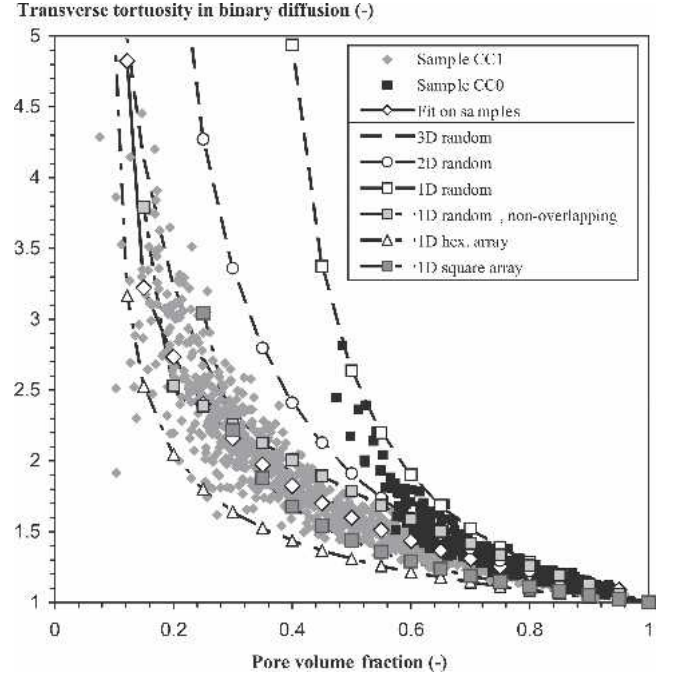

FIG. 5. Tortuosity–porosity correlation plots for bulk diffusion in transverse direction. Comparison of CMT data with established laws.

has been evaluated in a large number of subimages within the high-resolution 3D images of CC0 and CC1 (respectively 384 for sample CC0 and 1176 for sample CC1). These high-resolution subsamples have nearly the same physical size as the subsamples in the low-resolution images (i.e., ~0.05 mm³) so that correspondence between the microscopic correlation

established from these extracts and the property of the subsamples is valid.

The simulated longitudinal and transverse tortuosity of each subsample can be modeled in the form suggested by Tomadakis and Sotirchos,[32] which is an extension of Archie's law:

$$\eta_i = \eta_i^{\lim}\left(\frac{\epsilon_0 - \epsilon_p}{\epsilon - \epsilon_p}\right)^{\alpha_i} . \qquad (5)$$

Using a unit initial porosity, the identified coefficients for continuum and rarefied limits in parallel and transverse direction are shown in Table I. In all cases, the parameter fitting has been satisfactory, as indicated by the values of the R^2 correlation coefficient in Table I. It is worth comparing them with predictions for ideal media like one-dimensional (1D), two-dimensional (2D), and 3D random overlapping fiber arrangements.[21,32] and regular arrays in the bulk diffusion regime[16] [note that estimates in Knudsen regime cannot be cast into the form of Eq. (5) because of the "infinite horizon effect" that would yield an infinite value for D^{ref}]. Table I shows that the percolation porosity matches well the situation for 3D random fiber arrangements. The tortuosity limits in Knudsen regime lie between values for 1D and 3D random arrangements, and the characteristic exponent is close to the value for a 1D random arrangement. In the bulk diffusion regime, the limit tortuosity differs from all ideal predictions by only 9%; on the other hand, the characteristic exponent is neatly lower than all values for random media and higher than values for regular 1D arrays. However, the estimates for the regular arrays using Eq. (5) are not very accurate with respect to the original formulae.

From Figs. 4 and 5 and Table I, it is seen that there is not a large difference between samples CC0 and CC1 in Knudsen transport. On the other hand, for binary diffusion, an apparently more marked difference appears

between samples CC0 (very similar to a 1D random arrangement) and CC1 (much closer to a 3D random arrangement). However, the ordinate scale is linear in Fig. 5, while it is logarithmic for Knudsen diffusion (Fig. 4), denoting a much larger sensitivity to fiber arrangement in the latter regime.

2. Verification of the locally orthotropic character

The computational results yield three values of tortuosity, the lowest being close to one and defining the direction parallel to fibers, and the other two related to the perpendicular direction. These two values would be equal if the medium were locally orthotropic, but it is generally not the case. The error made when one considers the medium as orthotropic is quantified by the relative difference of these two values:

$$\mathrm{Error} = \frac{2|\eta_x - \eta_y|}{\eta_x + \eta_y} . \qquad (6)$$

Figure 6 is a histogram plot of the distribution of this error. It appears that sample CC0 is very close to obeying orthotropy, especially for continuum diffusion (the error average is 5%), and to a lesser extent for Knudsen diffusion (average error 22%). On the other hand, the discrepancy is stronger for CC1: 16% average error for binary transport and 72% average error for Knudsen diffusion. However, this does not have a strong influence on further computations because the anisotropy ratio is much larger than this relative difference.

3. Computation of the viscous flow permeabilities

The values of the permeabilities are obtained from microscale images by an averaging technique, performing a Stokes–Darcy change of scale. At low Reynolds numbers, it is sufficient to describe the fluid movement by Stokes equations:

TABLE I. Comparison of parallel and transverse tortuosity–porosity correlation parameters [Eq. (12)] obtained from high-resolution tomographic images with estimation on ideal fibrous media.[32]

|	Percolation porosity	Rarefied (Knudsen) regime		Continuum (ordinary) regime	
		Limit tortuosity	Exponent	Limit tortuosity	Exponent
Parallel					
Samples CC1 and CC0	0.04	0.817	0.126	1.0	0.107
Correlation coefficient R^2	...	0.95	0.95	0.99	0.99
2D random	0.11	1.149	0.954	1.0	0.521
1D random	0	0.549	0	1.0	0
Transverse					
Samples CC1 and CC0	0.04	1.411	1.047	1.09	0.465
Correlation coefficient R^2		0.93	0.93	0.99	0.99
3D random	0.037	1.444	0.921	1.0	0.661
2D random	0.11	1.780	1.005	1.0	0.785
1D random	0.33	1.747	1.099	1.0	0.707
1D hexagonal	0.093	...	...	1.0	0.335
1D square	0.215	...	...	1.0	0.358
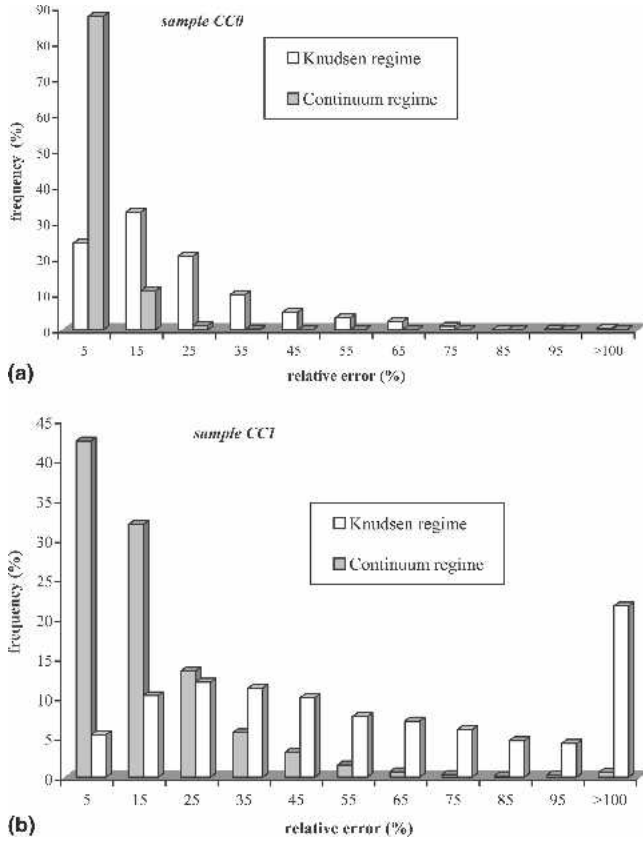
FIG. 6. Error distribution in considering the porous medium samples as orthotropic.

$$\begin{cases} -\mu\nabla^2\mathbf{v} + \nabla P = 0 & \text{in } \Omega_f \\ \nabla\cdot(\rho\mathbf{v}) = 0 & \text{in } \Omega_f \\ \mathbf{v} = 0 & \text{on } \partial\Omega_{fs} \end{cases} \quad . \quad (7)$$

Either by homogenization[33,34] or volume averaging,[35] the macroscopic behavior is proved to have the following form[36]:

$$\begin{cases} \nabla\cdot\langle\mathbf{v}\rangle = 0 \\ \langle\mathbf{v}\rangle = -\mu^{-1}\,\underline{\underline{B}}^{\text{eff}}\nabla\cdot\langle P\rangle^f \end{cases} , \quad (8)$$

where $\underline{\underline{B}}^{\text{eff}}$ is the mesoscopic permeability tensor (m^2). Equation (8) is the well-known Darcy law.[37] The numeric value of the permeability tensor may be obtained as an average of a closure tensor $\underline{\underline{F}}$:

$$\underline{\underline{B}}^{\text{eff}} = -\epsilon\langle\underline{\underline{F}}\rangle^f \quad , \quad (9)$$

where $\underline{\underline{F}}$, together with another vector closure variable $\mathbf{f}$, satisfies the following problem[38]:

$$\begin{cases} -\nabla\mathbf{f} + \nabla^2\,\underline{\underline{F}} = \underline{\underline{Id}} & \text{in } \Omega_f \\ \nabla\cdot\underline{\underline{F}} = 0 & \text{in } \Omega_f \\ \underline{\underline{F}} = 0 & \text{on } \partial\Omega_{fs} \quad , \\ \langle\mathbf{f}\rangle^f = 0 \\ + \text{ periodic BCs for } \mathbf{f} \text{ and } \underline{\underline{F}} \end{cases} \quad (10)$$

where BCs is boundary conditions.

The resolution has been implemented in a finite-volume solver[39,40] using an artificial compressibility transient scheme.

It has not been possible to perform as many computations as for diffusion because the large size of the subsamples required too much computer memory; rather, it was decided to select some subsamples and correlate permeabilities to existing expressions. Of particular interest is the correlation with effective binary diffusivities suggested by Johnson et al.[41] and Tomadakis and Robertson.[42] If one defines viscous flow tortuosity $\underline{\underline{\eta}}_v$ as

$$\underline{\underline{B}}^{\text{eff}} = \epsilon\frac{d_p^2}{32}\,\underline{\underline{\eta}}_v^{-1} \quad . \quad (11)$$

Then, summarizing the theory of Johnson,[41] the permeability–diffusivity correlation is given by the simple formula:

$$\eta_{v,i} = \frac{\eta_{b,i}}{M}\left(1 - \frac{\partial\ln\eta_{b,i}}{\partial\ln\epsilon}\right)^2 \quad , \quad (12)$$

where M is a constant close to 1. Recalling the extended Archie's law result [Eq. (5)], one has the following prediction:

$$\eta_{v,i} = \frac{\eta_{b,i}}{M}\left(1 + \frac{\alpha_{b,i}\epsilon}{\epsilon - \epsilon_p}\right)^2 \quad . \quad (13)$$

The best value found for M in the perpendicular direction is 0.95. Figure 7 is a plot of the tortuosities in the perpendicular direction predicted with Eq. (13) against the value computed directly. Even though some scatter is present, the agreement is satisfactory on a broad enough tortuosity range. On the other hand, results in parallel direction are somewhat underestimated through this method; they match more satisfactorily the correlations given by van der Westhuizen and Du Plessis[25] and by Tomadakis and Robertson[42] for random arrays of nonoverlapping parallel cylinders, as illustrated in Fig. 8. Also reported is the Kozeny relationship identified by Gutowski et al.[43] with a less satisfactory agreement.

E. First change of scale from ideal media: Local thermal conductivity

Heat conduction in carbon/carbon composites is strongly related to the precise nature of the carbon-based components (carbon fiber and pyrocarbon deposit), as well as to the gas. The thermal conductivity of carbon fibers is not easy to measure and is a subject of research.[44,45] Because precise measurements are lacking, we will refer to studies conducted by Sauder,[46] who deduced from electrical resistivity measurements
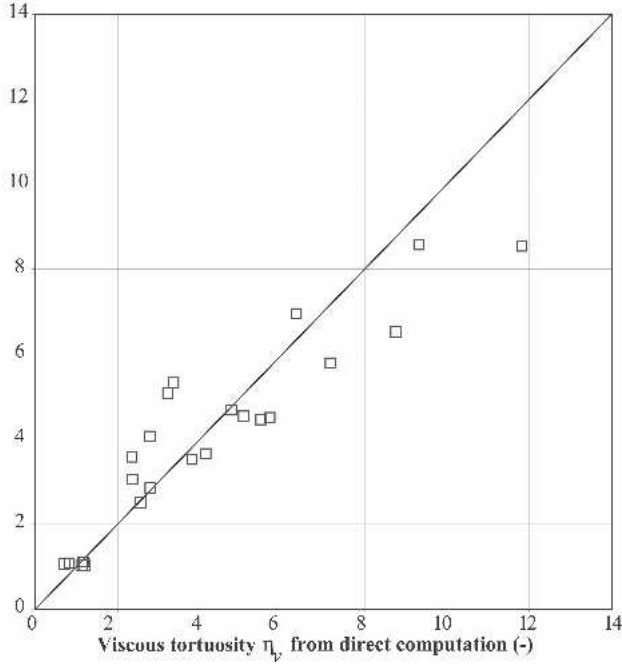
FIG. 7. Viscous transport tortuosity correlation plot between estimations from diffusivities and direct computations on some $100 \times 100 \times 100$ CMT images.

the longitudinal conductivity of carbon fibers. According to Jumel et al.,[47] the thermal conductivity of carbon fibers lies between 4 and 10.5 W m^{-1} K^{-1}. A value of 5 W m^{-1} K^{-1} has been retained for this study. The values determined by Jumel et al.[47,48] for the pyrocarbon deposit have been used. However, it is worth mentioning that there is a great variety of pyrocarbons with different nanotextures and consequently various thermal properties. The values taken for this work are summarized in Table II. Of course, the gas thermal conductivity is markedly lower than all other values, and its possible variation with pressure and temperature may be safely neglected.

It appears immediately that the heat conductivity of the solid phases is strongly anisotropic; moreover, the pyrocarbon deposit displays a cylindrical symmetry. This renders extremely difficult a direct simulation from CMT images, since the central axis of every fiber should be determined before assigning a local value of the heat conductivity to any voxel. So, it has been decided to provide a somewhat less satisfactory but readily feasible estimation based on a square array of parallel cylinders. The periodic unit cell is described in Fig. 9.

The longitudinal conductivity $\lambda_{i,\|}$ of the ith cell is directly given in analytical form by a law of mixtures (for conductances in parallel), where $\phi_{fi,i}$ is the fiber volume fraction:

$$\lambda_{i,\|} = \epsilon_i \times \lambda_{\text{gas}} + \phi_{fi,i} \times \lambda_{fi,\|} + (1 - \epsilon_i - \phi_{fi,i}) \times \lambda_{\text{pyC},\|} \quad . \tag{14}$$
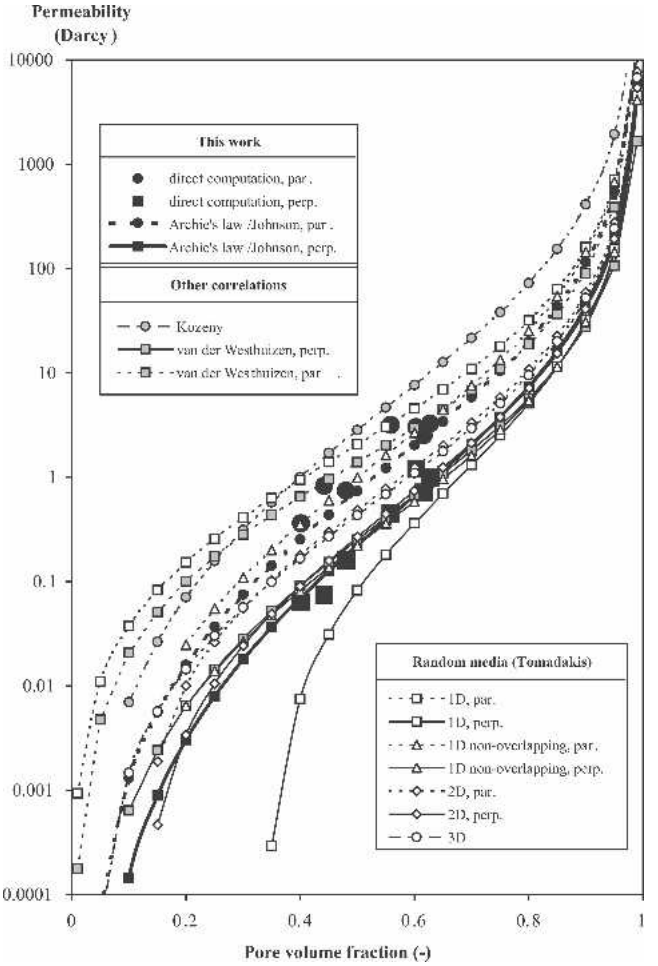

FIG. 8. Permeability estimates: comparison of direct computations from CMT images and established models.

TABLE II. Thermal conductivities of C/C composite components.

Component	Thermal conductivity (Wm^{-1}K^{-1})
Fiber	Longitudinal $\lambda_{fi,\|} = 20$
	Transverse $\lambda_{fi,\perp} = 4$
Pyrocarbon	Longitudinal $\lambda_{\text{pyC},\|} = 114$
	Radial $\lambda_{\text{pyC},\perp} = 44$
	Orthoradial $\lambda_{\text{pyC},\|} = 114$
Gas	Isotropic $\lambda_{\text{gas}} = 0.13$

In the raw state (sample CC0), the material is only made of fibers and pores so that $\phi_{fi,i}$ is simply $(1 - \epsilon_i)$. When the material is partially infiltrated, the local fiber fraction can be deduced from the local porosity by using the following proportionality relation:

$$\phi_{fi,i} = (1 - \epsilon_i) \frac{\langle \phi_{fi} \rangle}{\langle \phi_s \rangle} \quad , \tag{15}$$

where $\langle \phi_{fi} \rangle$ is the average fiber fraction in the material and $\langle \phi_s \rangle$ is the average solid fraction. The ratio between these two values is about 0.643 for CC1.

TABLE III. Simulated thermal conductivities obtained with the double change of scale procedure and measurements performed by Demange and Laizet.[56]

Sample	Method	Pore volume fraction ϵ (%)	In-plane heat conductivity $\lambda_{\parallel}$ (Wm^{-1}K^{-1})	Transverse heat conductivity $\lambda_{\perp}$ (Wm^{-1}K^{-1})
CC0	Computed in	72.7	0.62	0.43
	sub-samples	73.6	0.61	0.37
		73.4	0.57	0.40
	Computed, average	73.2	0.60	0.40
	Measured	73.0	0.60	0.38
CC1	Computed in	60.6	3.74	1.44
	sub-samples	58.7	3.74	2.05
		55.3	4.17	2.14
	Computed, average	58.2	3.88	1.88
	Measured	56.5	5.00	1.75

For the transverse conductivity of CC0, the following analytic equation of Perrins et al.[16] is suitable:

$$\frac{\lambda_{i,\perp}}{\lambda_{\text{gas}}} = 1 - \frac{2\phi_{fi,i}}{Q + \phi_{fi,i} - \dfrac{0.305827(\phi_{fi,i})^4 Q}{Q^2 - 1.402958(\phi_{fi,i})^8} - \dfrac{0.013362(\phi_{fi,i})^8}{Q}}$$

$$\text{with } Q = \frac{1 + \lambda_{fi,\perp}/\lambda_{\text{gas}}}{1 - \lambda_{fi,\perp}/\lambda_{\text{gas}}} \quad . \tag{16}$$

For CC1, constituted by three phases, the situation is more difficult. To partially circumvent this, the transverse conductivity of a square array of cylinders covered by an anisotropic deposit [see Fig. 9(a)] has been computed. The radius taken for the cylinders is 3.98 μm, and the deposit thickness is 2.6 μm (values assessed in Ref. 10 and confirmed by SEM micrographs). Computations have been performed for volume fraction of fibers lying between 0 and the percolation threshold for such an arrangement (i.e., 78.5%). The flux/force correlation method,[49,50] solved by a finite element software package, has been used. The results established for CC1 follow Eq. (16) if $\phi_{fi,i}$ lies below a given threshold $\phi_{fi,t}$, and in the converse case is:
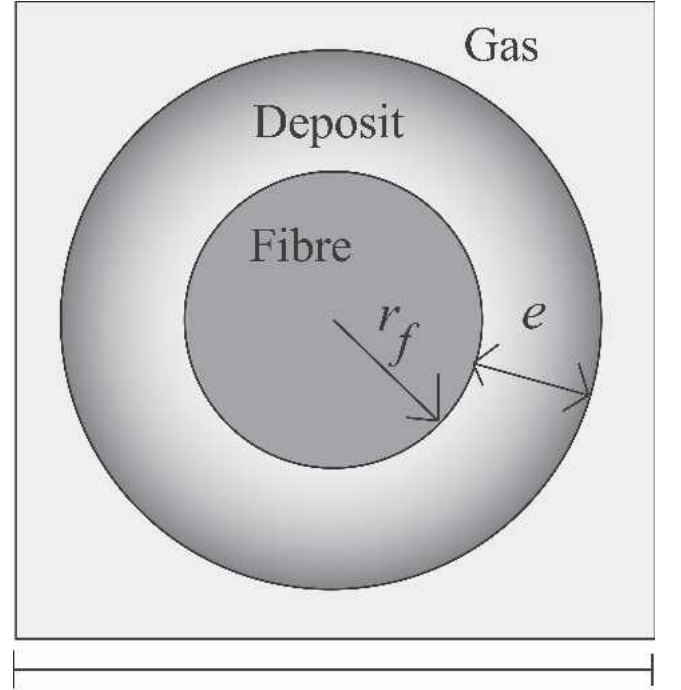
$$\lambda_{i,\perp} = \frac{-0.0141}{\phi_{fi,i} - \phi_{fi,t}} - 143.1(\phi_{fi,i})^2 + 137.9\phi_i^f - 12.8 \quad . \tag{17}$$

Expressions (16) and (17) are plotted in Fig. 10(a). They are converted into a porosity–conductivity correlation for CC1 as plotted in Fig. 10(b).
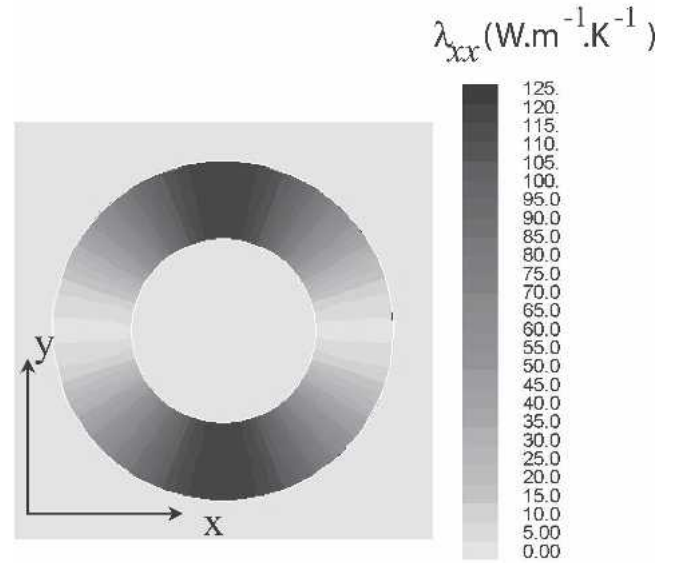
F. Second change of scale: Computation of "large scale" properties

1. Strategy

The second change of scale consists of determining the effective property in large-scale images, the size of

(a)

(b)

FIG. 9. Periodic unit cell for small-scale thermal computations: (a) scheme illustrating the cylindrical symmetry of heat conductivity in the pyrocarbon deposit and (b) horizontal thermal conductivity (λ_{xx}) field in the image.

which is broad enough to ensure adequate representation of the whole porous medium. Whatever the property, this is computed by the same method, since all integrated expressions have the same flux–force formalism.

Details of the application of the volume averaging method[35] to the process of heat conduction in two- and three-phase systems are described in Ref. 51. In this
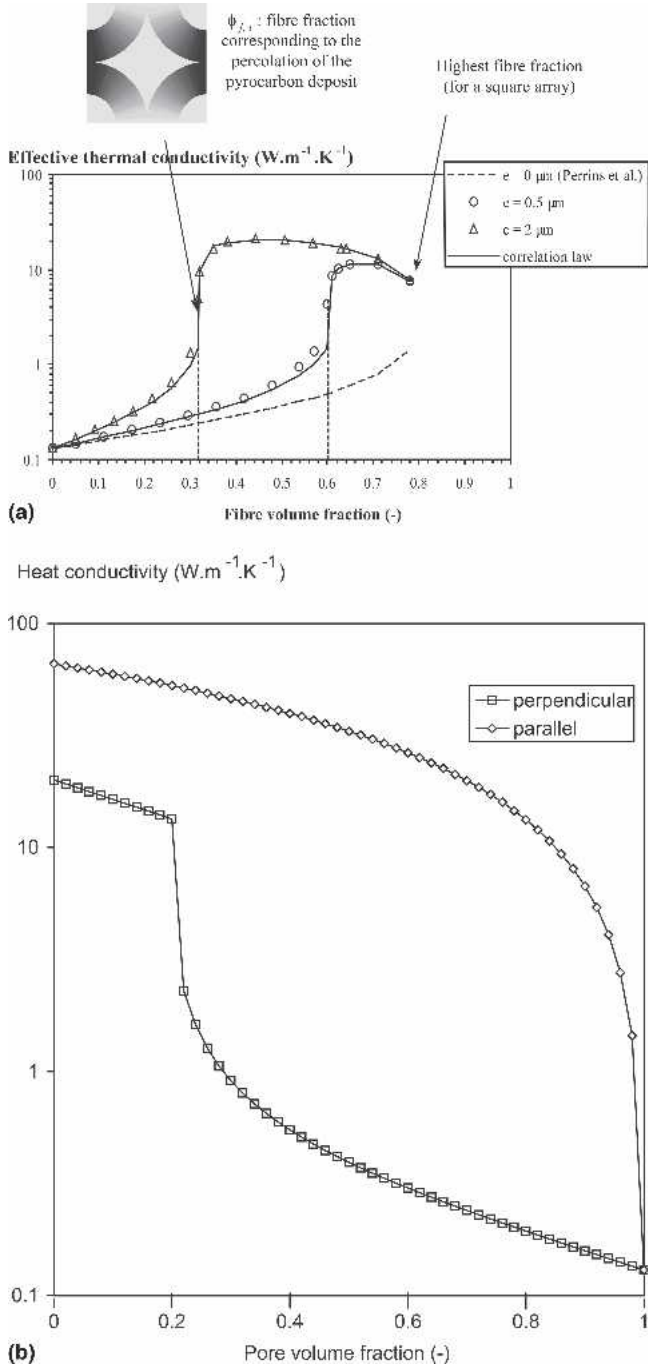
FIG. 10. Microscopic correlations for the transverse thermal conductivity of a square array of cylinders covered by an anisotropic layer: (a) conductivity as a function of Fiber volume fraction for various deposit thicknesses and (b) conductivity as a function of pore volume for sample CC1.

work, focused on the first change of scale, spherical conductivity tensors are considered for each phase. However, the change of scale procedure for another diffusive process, namely the single phase flow in heterogeneous porous media (two-region media and heterogeneous porous media with continuously varying properties), leads to similar results in which the permeability tensors consid-

ered are not necessarily spherical.[52] The extension of their results to multiregion models is rather straightforward. In all the works cited above, the averaging process and the closure are based upon an equilibrium assumption, assuming that a single large-scale equation—therefore a single large-scale effective property—is sufficient for a correct macroscopic description of the phenomena.

The averaging process[53] leads to the following closure problem:

$$
\begin{cases}
\underline{\underline{\lambda}}_i : \nabla\nabla\mathbf{b}_i = 0 & \text{on } \Omega_i, \quad i = 1\cdots,n \\
\mathbf{n}_{ij}\cdot[\underline{\underline{\lambda}}_i\cdot\nabla\mathbf{b}_i + \underline{\lambda}_i] = \mathbf{n}_{ij}\cdot[\underline{\underline{\lambda}}_j\cdot\nabla\mathbf{b}_j + \underline{\lambda}_j] & \text{on } \partial\Omega_{ij} \\
\mathbf{b}_i = \mathbf{b}_j & \text{on } \partial\Omega_{ij} \\
\{\mathbf{b}\} = \dfrac{1}{\Omega}\sum_i\int_{\Omega_i}\mathbf{b}_i dV = 0 \\
+ \text{ periodic BCs}
\end{cases}
,
$$

(18)

where Ω is the large-scale averaging volume composed of n regions (Ω_i, $i = 1, \ldots, n$). The tensor $\underline{\underline{\lambda}}_i$ is the conductivity tensor for the ith region (Ω_i), and $\mathbf{b}_i$ is the closure variable defined in Ω_i. The interface between regions Ω_i and Ω_j is denoted $\P\Omega_{ij}$. The large-scale average of a quantity ψ is defined as

$$
\{\psi\} = \frac{1}{\Omega}\int_\Omega \psi dv \quad .
$$

(19)

The effective conductivity tensor is given explicitly as a function of the closure variable $\mathbf{b}$ and local conductivities resulting from the first change of scale:

$$
\underline{\underline{\lambda}}^* = \{\underline{\underline{\lambda}}\} + \{\underline{\tilde{\lambda}} : \nabla\mathbf{b}\} \quad ,
$$

(20)

where $\underline{\tilde{\lambda}}$ is the conductivity deviation resulting from the decomposition of the local conductivity as $\underline{\lambda} = \{\underline{\lambda}\} + \underline{\tilde{\lambda}}$.

The closure problem has been solved numerically using a continuous-flux, locally conservative finite volume method with a 27-point scheme proposed by Edwards and Rogers.[54] Indeed, the typically used seven-point stencil cannot be used in this particular case of full tensor local conductivity. A thorough description of the method can be found in Cherblanc et al.[55]

At advanced stages of densification, the pore space exhibits only one degree of heterogeneity with respect to gas transport, since the contribution of micro-pores vanishes because of size reduction and of connectivity loss. Thus, a simple change of scale can be designed for the computation of gas transport properties of such a material. However, since heat transport is not ensured by the pore space, this assumption is not true for the computation of thermal conductivity. For the computation of gas transport properties, 3 extracts with edge size equal to 200 voxels were selected within low-resolution images of CC1b and CC2. Subimages were segmented to separate the solid phase from the pore space. Effective

diffusivities were then computed using the random-walk algorithm described previously. For the effective permeability tensor, the algorithm developed by Anguy and Bernard[39,40] presented above was used again.

The results have been compared to experimental measurements as far as possible; data were available on thermal conductivity[56] and on pure gas transport.[57,58] The latter properties have been determined at LCTS on a simple traditional experimental setup, inspired by Refs. 15 and 59 using argon with a calibrated gas flow meter, a pressure difference gauge, and a terminal low-pressure regulation unit (vacuum pump and vane). From steady-state flow versus pressure difference curves obtained at various average pressures, the permeability and Knudsen diffusion coefficient were recovered.[60,61]

2. Results

Figure 11 is a plot of computed Knudsen diffusivities as compared to experimental determinations performed at LCTS; at the macroscale, the parallel and perpendicular directions now refer to the cloth stacking and not to the fiber orientations. The calculated values are in qualitative agreement with the experiments, but there is a tendency to underestimate at high porosities. Many reasons may be put forward. First, the experimental determinations are of limited reliability because of the small values of the flows involved. Also, the CMT-based estimation relies on the assumption of linear relationship between local grayscale level and density, which is not exactly verified because of the presence of a certain amount of phase contrast; such an artifact is more pronounced for the most porous samples.

Even if there is no experimental data available on binary diffusion, it is of interest to investigate the effect of the Knudsen number on the effective tortuosity.
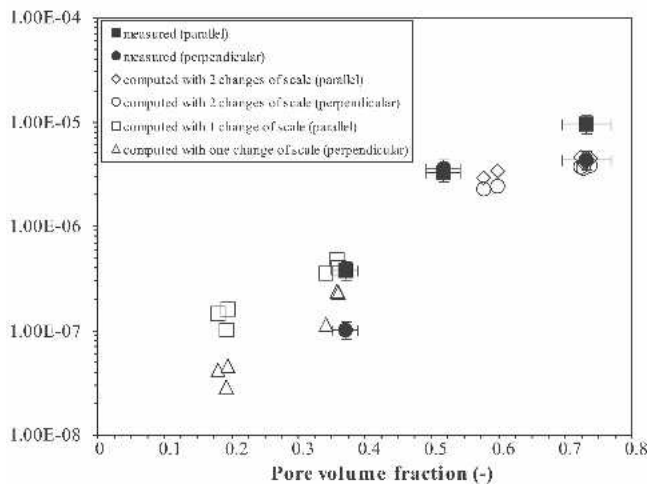
Figure 12 is a plot of the estimated values for samples CC0 and CC1 showing (i) a very low value for all tortuosities, as can be expected in a very porous medium and (ii) a monotonous evolution for CC1 while there is a hump for CC0. The latter behavior had been reported in Ref. 22 for regular unidirectional arrays of cylinders with large porosity. A direct interpretation for this is that the mean free path is drastically increased when going from the transitional to the rarefied regime because a very open structure provides longer free paths; indeed, when it is too open, convergence of the effective transport law (i.e., flux/gradient relationship) to classical Knudsen diffusion is not even ensured.

Figure 13 is a plot of computed versus measured permeabilities, showing qualitative agreement, and a marked discrepancy for high-porosity samples. The aforementioned limitations on the image-based evaluation method appear again, more or less in the same way as they did for Knudsen diffusion.

Figure 14 is a plot of computed versus measured heat conductivities, showing excellent agreement in both directions.

Summarizing the results of Figs. 11, 13, and 14, it can be said that the porous medium family corresponding to the C fiber preform at various stages of infiltration has been correctly assessed on all transport (and geometrical) properties. Of these transport properties, Knudsen transport has been found to be the most sensitive to infiltration, followed by viscous flow and finally by thermal conductivity. This is in agreement with the physicist's intuition: first, thermal conductivity contrasts are known to be low, e.g., compared to electrical conductivity or any other property; second, Knudsen transport displays in many media a stronger tortuosity increase with diminishing porosity than the other gas transport parameters because of the rapid view-factor reduction for direct transport as soon as a conducting medium is not straight. This

FIG. 11. Comparison of computed and experimental values of Knudsen flow coefficients.
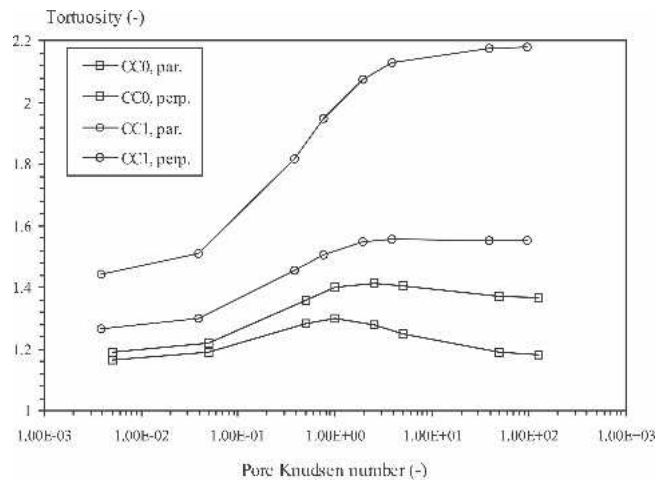

FIG. 12. Tortuosity versus pore Knudsen number, as computed on samples CC0 and CC1.
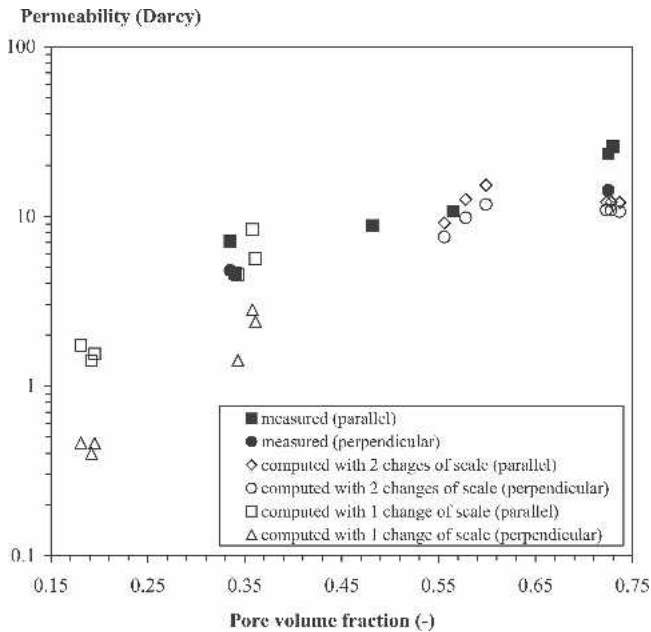
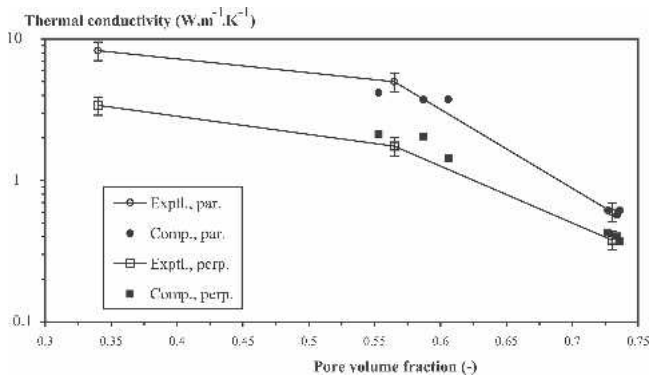FIG. 13. Comparison of computed and experimental values of permeabilities.

FIG. 14. Comparison of computed and experimental values of thermal conductivities.

last fact is confirmed here again both numerically and experimentally.

IV. CONCLUSION AND OUTLOOK

Raw and partially infiltrated carbon–carbon composite preforms were scanned by high-resolution synchrotron radiation x-ray CMT. The quality of the images was assessed on geometrical quantities in a previous work.[10] Here, the images of the pore space were produced at two distinct resolutions and used for the computation of transport properties: heat conductivity, binary gas diffusivities, Knudsen diffusivities, and viscous flow permeabilities. It is the first attempt to perform such a simultaneous evaluation directly from tomographic scans on C/C composites, mostly because (i) very high-scale 3D images with adequate phase identification were not previously available, and (ii) the bimodal nature of the

samples implies the development of a double-change-of-scale strategy.

The numerical evaluation of fiber-scale gas diffusivities in continuous and rarefied regime in the studied media is in fair agreement with estimates on ideal media like 1D, 2D, and 3D random fiber arrays. Viscous flow permeabilities were also assessed and compared to available correlations for 1D random fiber arrangements, showing excellent agreement with the van der Westhuizen–Du Plessis[25] and Tomadakis[42] models in the parallel direction, and with the Tomadakis model in the perpendicular direction. Further work at this scale concerns primarily the direct computation of thermal conductivity or diffusivity: this requires a separate segmentation of fibers and matrix, with a local assignment of material principal axes of anisotropy; this work is currently under way.

Computations on a larger scale were carried out for all transport properties; it was possible to directly compare the results with experimental data acquired on the same materials for Knudsen diffusivity, viscous flow permeability, and thermal conductivity. Despite an excellent agreement on all properties, many improvements may be suggested. First, images of high-porosity samples do not completely obey the grayscale–porosity correlation because of phase contrast: tomographs taken at the same resolution with a classical (i.e., not coherent nor monochromatic) x-ray source would be better.

Second, concerning gas transport, there is a need for a unified solver, able to manage high- and low-porosity samples in the same way. This could be achieved for viscous transport by writing down a Stokes–Brinkman microscopic problem, followed by the traditional change-of-scale procedure. This is also under way.

Third, replacing the provided analytical estimates for fiber-scale thermal conductivity by estimates based on the results of a full numerical computation (as mentioned above) would greatly increase the confidence in the quality of this CMT-based approach.

Taking note of these improvement suggestions, it is claimed here that CMT-based simulations are a powerful tool for the assessment of all properties of interest in C/C composite preforms during infiltration, which is of great importance in CVI process modeling. By combining process-scale approaches and the correlations obtained in past[10] and present works, it is possible to carry out a multi-scale simulation. Repeating the procedure on several fiber arrangements would allow them to be compared with one another in the sense of "infiltrability," that is, of the predisposition to receive as much matrix as possible under given conditions.

Finally, it is also possible to develop numerical methods for the detailed simulation of in-pore matrix deposition; utilizing them in a suitable double-change-of-scale strategy would also allow the notion of "infiltrability" to be quantitatively assessed. This is yet another work in progress.

List of symbols

Symbol	Signification	Unit
a	Sub-sample edge length	m, μm
$\mathbf{b}$	Closure variable	m
$\underline{B}$	Permeability	m^2, μm^2
d_p	Pore diameter	m, μm
$\underline{\underline{D}}$	Diffusion coefficient	m^2 s^{-1}
$\mathbf{f}, \underline{F}$	Closure variables	m, m^2
G	Image grayscale value	…
$\underline{\underline{Id}}$	Identity tensor	…
M	Corrective constant in Eq. (12)	…
N	Distribution number	…
$\mathbf{n}$	Normal vector	
P	Pressure	Pa
Kn	Knudsen number	…
Q	Auxiliary variable; see Eq. (16)	
$\mathbf{v}$	Velocity	m s^{-1}
α	Characteristic exponent for tortuosity-porosity correlations	…
ϵ	Porosity (volume fraction)	…
$\underline{\underline{\eta}}$	Tortuosity factor	…
$\underline{\underline{\lambda}}$	Thermal conductivity	W m^{-1} K^{-1}
μ	Viscosity	Pa·s
ρ	Density	kg m^{-3}
ϕ_{fi}	Fiber volume fraction	…
Ψ	Any material property	
Ω	Space domain	[m^3]

Superscripts and subscripts

Symbol	Signification
$\langle \bullet \rangle$	Intermediate-scale average
$\langle \bullet \rangle^\epsilon$	Porosity-distribution-based average
$\langle \bullet \rangle^f$	Intrinsic fluid average
$\{ \bullet \}$	Large-scale average
$\bullet^{lim}$	Limiting value
$\bullet^{ref}$	Reference
$\bullet^{eff}$	Effective value
$\bullet_b$	Relative to binary diffusion˘
$\bullet_f$	Relative to fluid phase
$\bullet_{fi}$	Relative to fiber
$\bullet_{fs}$	Relative to fluid–solid interphase
$\bullet_{gas}$	Relative to gas phase
$\bullet_p$	Relative to percolation threshold
$\bullet_{pyC}$	Relative to pyrocabon
$\bullet_s$	Relative to solid phase
$\bullet_v$	Relative to viscous flow
$\bullet_{x, y, \text{ or } z}$	Relative to x, y, or z direction
$\bullet_0$	Initial state
$\bullet_{//}$	Relative to parallel direction
$\bullet_\perp$	Relative to perpendicular (transverse) direction

REFERENCES

1. R. Naslain and F. Langlais: Fundamental and practical aspects of the chemical vapor infiltration of porous materials. *High Temp. Sci.* **27,** 221 (1990).
2. T.M. Besmann, B.W. Sheldon, R.A. Lowden, and D.P. Stinton: Vapor-phase fabrication and properties of continuous-filament ceramic composites. *Science* **253,** 1104 (1991).
3. S. Vaidyaraman, W.J. Lackey, P.K. Agrawal, and T.L. Starr: 1-D model for forced-flow-thermal gradient chemical vapor infiltration process for carbon/carbon composites. *Carbon* **34,** 1123 (1996).
4. J.Y. Ofori and S.V. Sotirchos: Structural model effects on the predictions of CVI models. *J. Electrochem. Soc.* **143,** 1962 (1996).
5. N. Reuge and G.L. Vignoles: Modeling of isobaric–isothermal chemical vapor infiltration: Effects of reactor control parameters on a densification. *J. Mater. Proc. Technol.* **166,** 15 (2005).
6. G.L. Vignoles, N. Nadeau, C-M. Brauner, J-F. Lines, and J-R. Puiggali: The notion of densification front in CVI processing of CMCs. *Ceram. Eng. Sci. Proc.* **26,** 187 (2005).
7. G.L. Vignoles, J-M. Goyhénèche, P. Sébastian, J-R. Puiggali, J-F. Lines, J. Lachaud, P. Delhaès, and M. Trinquecoste: The film-boiling densification process for C/C composite fabrication: From local scale to overall optimization. *Chem. Eng. Sci.* **61,** 5336 (2006).
8. N. Nadeau, G.L. Vignoles, and C-M. Brauner: Analytical and numerical study of the densification of carbon/carbon composites by a film-boiling chemical vapor infiltration process. *Chem. Eng. Sci.* **61,** 7509 (2006).
9. G.L. Vignoles: Modelling of CVI Processes, in *Proc. CIMTEC 2006,* edited by P. Vicenzini, *Adv. Sci. Technol.* **50** (Trans Tech Publications, Zürich, 2006), pp. 97–106.
10. O. Coindreau and G.L. Vignoles: Assessment of geometrical and transport properties of a fibrous C/C composite preform using x-ray computerized micro-tomography. Part I: Image acquisition and geometrical properties. *J. Mater. Res.* **20,** 2328 (2005).
11. L.M. Russell, L.F. Johnson, and D.P.H. Hasselman: Thermal conductivity/diffusivity of silicon carbide whisker reinforced mullite. *J. Am. Ceram. Soc.* **70,** C226 (1987).
12. H. Tawil, L.D. Bentsen, S. Baskaran, and D.P.H. Hasselman: Thermal diffusivity of chemically vapor deposited silicon carbide reinforced with silicon carbide or carbon fibres. *J. Mater. Sci.* **20,** 3201 (1985).
13. D.J. Jaklitsch and J.W. Walkinshaw: Flash pulse measurement for off-axis thermal conductivity of carbon composite materials. *Ind. Eng. Chem. Res.* **27,** 702 (1988).
14. D.J. Skamser, D.P. Bentz, R.T. Coverdale, M.S. Spotz, N. Martys, L.H. Jennings, and D.L. Johnson: Calculation of the thermal conductivity and gas permeability in a uniaxial bundle of fibers. *J. Am. Ceram. Soc.* **77,** 2669 (1994).
15. T.L. Starr and N. Hablutzel: Measurement of gas transport through fiber preforms and densified composites for chemical vapor infiltration. *J. Am. Ceram. Soc.* **81,** 1298 (1998).
16. W.T. Perrins, D.R. McKenzie, and R.C. McPhedran: Transport properties of regular arrays of cylinders. *Proc. R. Soc. London A* **369,** 207 (1979).
17. G.W. Milton: Bounds on the transport and optical properties of a two-component composite material. *J. Appl. Phys.* **52,** 5294 (1981).
18. D.S. Tsai and W. Strieder: Effective conductivities of random fibre beds. *Chem. Eng. Commun.* **40,** 207 (1986).

19. I. Kim and S. Torquato: Determination of the effective conductivity of heterogeneous media by brownian motion simulation. *J. Appl. Phys.* **68,** 3892 (1990).

20. M.M. Tomadakis and S.V. Sotirchos: Ordinary and transition regime diffusion in random fibre structures. *AIChE J.* **39,** 397 (1993).

21. M.M. Tomadakis and S.V. Sotirchos: Transport properties of random arrays of freely overlapping cylinders with various orientation distributions. *J. Chem. Phys.* **98,** 616 (1993).

22. F. Transvalidou: Diffusion of gases in structures of multifilamentous fibers, Ph.D. Thesis, University of Rochester, New York (1995).

23. A.S. Sangani and A. Acrivos: Slow flow past periodic arrays of cylinders with application to heat transfer. *Int. J. Multiphase Flow* **8,** 193 (1982).

24. J.F. McCarthy: Analytical models for the effective permeability of sand-shale reservoirs. *Geophys. Int. J.* **105,** 513 (1991).

25. J. van der Westhuizen and J.P. du Plessis: An attempt to quantify fibre bed permeability utilizing the phase average navier-stokes equation. *Composites Part A* **27,** 263 (1996).

26. P. Cloetens, R. Barrett, J. Baruchel, J.P. Guigay, and M. Schlenker: Phase objects in synchrotron radiation hard x-ray imaging. *J. Phys. D* **29,** 133 (1996).

27. O. Coindreau, G.L. Vignoles, and P. Cloetens: Direct 3D microscale imaging of carbon-carbon composites with computed holotomography. *Nucl. Instrum. Meth. Phys. Res. B* **200**, 308 (2003).

28. M. Jonard: Study of the pore network in tridimensional textures (Engineering report, Snecma, Le Haillan, France, 2001), in French.

29. G.L. Vignoles: Modelling binary, Knudsen and transition regime diffusion inside complex porous media. *J. Physique IV* **C5,** 159 (1995).

30. W.G. Pollard and R.D. Present: On gaseous self-diffusion in straight cylindrical pores. *Phys. Rev.* **73,** 762 (1948).

31. O. Coindreau, G.L. Vignoles, and J-M. Goyhénèche: Multiscale x-ray CMT of C/C composites: A tool for properties assessment. *Ceram. Trans.* **175,** 77 (2005).

32. M.M. Tomadakis and S.V. Sotirchos: Effects of fiber orientation and overlapping on Knudsen, transition, and ordinary regime diffusion in fibrous structures, in *Chemical Vapor Deposition of Refractory Metals and Ceramics II,* edited by T.M. Besmann, B.M. Gallois, and J.W. Warren (Mater. Res. Soc. Symp. Proc. **250,** Pittsburgh, PA, 1992*),* pp. 221–226.

33. E. Sanchez-Palencia: Non-homogeneous media and vibration theory, in *Lecture Notes in Physics* **127** (Springer, Berlin, 1980).

34. A. Bensoussan, J-L. Lions, and G. Papanicolaou: *Asymptotic Analysis for Periodic Structures* (North-Holland Publishing Company, Amsterdam, The Netherlands, 1978).

35. S. Whitaker: Diffusion and dispersion in porous media. *AIChE J.* **13,** 420 (1967).

36. J. Barrère, O. Gipouloux, and S. Whitaker: On the closure problem for Darcy's law. *Trans. Porous Media* **7,** 209 (1992).

37. H.P.G. Darcy: *The Public Springs of the City of Dijon* (Victor Dalmont, Paris, France, 1856).

38. M. Quintard and S. Whitaker: Transport in ordered and disordered porous media: Volume-averaged equations, closure problems, and comparison with experiment. *Chem. Eng. Sci.* **48,** 2537 (1993).

39. Y. Anguy, D. Bernard, and R. Ehrlich: The local change of scale method for modelling flow in natural porous media (I): Numerical tools. *Adv. Water Res.* **17,** 337 (1994).

40. D. Bernard: Using the volume averaging technique to perform the first change of scale for natural random porous media, in *Advanced Methods for Groundwater Pollution Control*, Courses and Lectures No. 364, edited by G. Gambolati and G. Verri (Springer-Verlag, Wien, New-York, 1995).

41. D.L. Johnson, J. Koplik, and L.M. Schwartz: New pore-size parameter characterizing porous media. *Phys. Rev. Lett.* **57,** 2564 (1986).

42. M.M. Tomadakis and T.J. Robertson: Viscous permeability of random fiber structures: Comparison of electrical and diffusional estimates with experimental and analytical results. *J. Compos. Mater.* **39,** 163 (2005).

43. T.G. Gutowski, Z. Cai, S. Bauer, D. Boucher, J. Kingery, and S. Wineman: Consolidation experiments for laminate composites. *J. Composite Mater.* **21,** 650 (1987).

44. N.C. Gallego, D.D. Edie, B. Nysten, J.P. Issi, J.W. Treleaven, and G.V. Deshpande: The thermal conductivity of ribbon-shaped carbon fibers. *Carbon* **38,** 1003 (2000).

45. C. Pradère: Thermal and thermomechanical characterization of fibers up to very high temperatures, Ph.D. Thesis, University Bordeaux I (2003), in French.

46. C. Sauder: High-temperature structure-properties relationship in carbon fibers and matrices, Ph.D. Thesis, University Bordeaux I, 2477, (2001), in French.

47. J. Jumel, J-C. Krapez, F. Lepoutre, F. Enguehard, D. Rochais, G. Neuer, and M. Cataldi: Microscopic thermal characterization of C/C and C/C-SiC composites, in *28th Annual Review of Progress in QNDE*, edited by D.O. Thomson and D.E. Chimenti, Brunswick (USA), (American Institute of Physics, Melville, NY, 2001).

48. J. Jumel, F. Lepoutre, J-P. Roger, G. Neuer, M. Cataldi, and F. Enguehardt: Microscopic thermal characterization of composites. *Rev. Sci. Instrum.* **74,** 537 (2003).

49. D.M. Staicu, D. Jeulin, M. Beauvy, M. Laurent, C. Berlanga, N. Negrello, and D. Gosset: Effective thermal conductivity of heterogeneous materials: Calculation methods and application to different microstructures, *High Temp. High Press.* **33,** 293 (2001).

50. G.E. Youngblood, D.J. Senor, R.H. Jones, and S. Graham: The transverse conductivity of 2D-SiC$_f$/SiC composites. *Comp. Sci. Technol.* **62,** 1127 (2002).

51. I. Nozad, R.G. Carbonell, and S. Whitaker: Heat conduction in multiphase systems—I. Theory and experiment for two-phase systems. *Chem. Eng. Sci.* **40,** 843 (1985).

52. M. Quintard and S. Whitaker: Single phase flow in porous media: Effect of local heterogeneities. *J. Méc. Théor. Appl.* **6,** 691 (1987).

53. M. Quintard and S. Whitaker: Transport in ordered and disordered media II: Generalized volume-averaging. *Transport Porous Media* **14,** 179 (1994).

54. M.G. Edwards and C.F. Rogers: A flux continuous scheme for the full tensor pressure equation, in *Proceeding 4th European Conference on the Mathematics of Oil Recovery* **D** (European Association of Geoscientists and Engineers, Houten, The Netherlands, 1994).

55. F. Cherblanc, A. Ahmadi, and M. Quintard: Two-medium description of dispersion in heterogeneous porous media: calculation of macroscropic properties. *Water Resour. Res.* **39,** 1154 (2003).

56. D. Demange and J.C. Laizet: Measurements of thermal conductivity in raw and infiltrated preforms (Technical Report No. RT 1/03519 DMSC, Commissariat à l'Energie Atomique, Le Ripault, France, 2000), in French.

57. M-A. Dourges, O. Coindreau, N. Reuge, G.L. Vignoles, and R. Pailler: Characterization of complex solid porous media, in *Proceedings of Porous media Workshop* edited by L. Tadrist (IUSTI, Marseilles, France, 2001), in French.

58. O. Coindreau and G.L. Vignoles: Computing structural and transport properties of C/C composites from 3D tomographic images. *Mater. Sci. Forum* **455–456,** 751 (2004).

59. D.G. Huizenga and D.M. Smith: Knudsen diffusion in random assemblages of uniform spheres. *AIChE J.* **32,** 1 (1986).

60. L.J. Klinkenberg: The permeability of porous media to liquids and gases, in *Drilling and Production Practice,* 1947, (American Petroleum Institute, Washington, DC), pp. 200–214.

61. Y-S. Wu, K. Pruess, and P. Persoff: Gas flow in porous media with Klinkenberg effects, *Trans. Porous Media* **32,** 117 (1998).